Biomimetic 4D printing

A. Sydney Gladman[1,2][†], Elisabetta A. Matsumoto[1,2][†], Ralph G. Nuzzo[3], L. Mahadevan[1,2,4]★ and Jennifer A. Lewis[1,2]★

Shape-morphing systems can be found in many areas, including smart textiles[1], autonomous robotics[2], biomedical devices[3], drug delivery[4] and tissue engineering[5]. The natural analogues of such systems are exemplified by nastic plant motions, where a variety of organs such as tendrils, bracts, leaves and flowers respond to environmental stimuli (such as humidity, light or touch) by varying internal turgor, which leads to dynamic conformations governed by the tissue composition and microstructural anisotropy of cell walls[6-10]. Inspired by these botanical systems, we printed composite hydrogel architectures that are encoded with localized, anisotropic swelling behaviour controlled by the alignment of cellulose fibrils along prescribed four-dimensional printing pathways. When combined with a minimal theoretical framework that allows us to solve the inverse problem of designing the alignment patterns for prescribed target shapes, we can programmably fabricate plant-inspired architectures that change shape on immersion in water, yielding complex three-dimensional morphologies.

Plants exhibit hydration-trigged changes in their morphology due to differences in local swelling behaviour that arise from the directional orientation of stiff cellulose fibrils within plant cell walls[6-10]. Emerging pathways for mimicking these dynamic architectures incorporate materials that can respond to external stimuli, such as shape memory alloys[11,12] and swellable hydrogel composites[13,14], and are assembled by methods such as four-dimensional (4D) printing[11,15] and self-folding origami[16-18]. For example, recent efforts to create plant-inspired, shape-changing structures[10] have employed differential swelling in isotropic or composite bilayers and hinges[8,13,14,16]. However, none of these approaches enable shape change using a single material patterned in a one-step process, nor do they utilize a predictive model capable of tackling both the forward and inverse design problems (Supplementary Text and Supplementary Figs 1 and 2). Here, we develop a biomimetic hydrogel composite that can be 4D printed into programmable bilayer architectures patterned in space and time, which are encoded with localized swelling anisotropy that induces complex shape changes on immersion in water.

Our hydrogel composite ink is composed of stiff cellulose fibrils embedded in a soft acrylamide matrix, which mimics the composition of plant cell walls. The composite architectures are printed using a viscoelastic ink that contains an aqueous solution of N,N-dimethylacrylamide (or N-isopropylacrylamide for reversible systems), photoinitiator, nanoclay, glucose oxidase, glucose, and nanofibrillated cellulose (NFC). The constituents serve different purposes: the clay particles are a rheological aid, inducing the desired viscoelastic behaviour required for direct ink writing[19] (Supplementary Fig. 3); glucose oxidase and glucose minimize oxygen inhibition during the ultraviolet curing process by scavenging ambient oxygen[20], thereby improving polymerization in the printed filamentary features ($\sim$100 µm to 1 mm in diameter) to yield mechanically robust structures; the wood-derived cellulose fibrils, which bundle into microfibrils with high aspect ratio ($\sim$100), serve as stiff fillers ($E > 100$ GPa; ref. 21). After printing under ambient conditions, the acrylamide monomer is photopolymerized and physically crosslinked by the nanoclay particles, producing a biocompatible hydrogel matrix that swells readily in water[22]. (See Methods for further details.)

The efficacy of our biomimetic 4D printing (bio-4DP) method relies on the ability to deterministically define the elastic and swelling anisotropies by local control of the orientation of cellulose fibrils within the hydrogel composite. During printing, these fibrils undergo shear-induced alignment[23] as the ink flows through the deposition nozzle[24], which leads to printed filaments with anisotropic stiffness, and, hence, swelling behaviour in the longitudinal direction (along the filament length, as defined by the printing path) compared to the transverse direction (Fig. 1a). Significant cellulose fibril alignment is directly observed in the printed samples compared to isotropic cast sheets of the same material (Fig. 1b–d). Fourier analysis quantifies the relative alignment between cast and printed specimens, which indicates a clear directionality peak in the latter case (Fig. 1e and Supplementary Fig. 4). Thus, the printed architectures exhibit a fourfold difference in longitudinal and transverse swelling strains of $\alpha_{\parallel} \sim 10\%$ and $\alpha_{\perp} \sim 40\%$, respectively (Fig. 1f,g). Likewise, this signature of anisotropy is present in the elastic moduli, with longitudinal and transverse values of $E_{\parallel} \sim 40$ kPa and $E_{\perp} \sim 20$ kPa, respectively (Supplementary Figs 5 and 6). The extent of shear-induced alignment, and, hence, the magnitude of the anisotropic swelling, depends on the nozzle diameter and printing speed. For a fixed printing speed, the shear forces that align the cellulose fibrils scale inversely with nozzle size, as reflected in the observed longitudinal and transverse swelling strains (Fig. 1f).

Harnessing anisotropic swelling allows precise control over the curvature in bilayer structures[9,25]. Quantifying this requires a mathematical model for the mechanics of anisotropic plates and shells, which combines aspects of the classical Timoshenko model for thermal expansion in bilayers[26] with a tailored metric-driven approach[9,25] that employs anisotropic swelling to control the embedding of a complex surface. In a bilayer system, differential swelling between the top and bottom layers induces curvature, because the layers are forced to remain in contact along the entire midplane. Thereby, the displacements, integrated from the swelling

[1]John A. Paulson School of Engineering and Applied Sciences, Harvard University, 29 Oxford Street, Cambridge, Massachusetts 02138, USA. [2]Wyss Institute for Biologically Inspired Engineering, Harvard University, 60 Oxford Street, Cambridge, Massachusetts 02138, USA. [3]School of Chemical Sciences, University of Illinois Urbana-Champaign, Urbana, Illinois 61801, USA. [4]Departments of Physics and Organismic and Evolutionary Biology, and Kavli Institute for NanoBio Science and Technology, Harvard University, 29 Oxford Street, Cambridge, Massachusetts 02138, USA. [†]These authors contributed equally to this work. *e-mail: lm@seas.harvard.edu; jalewis@seas.harvard.edu
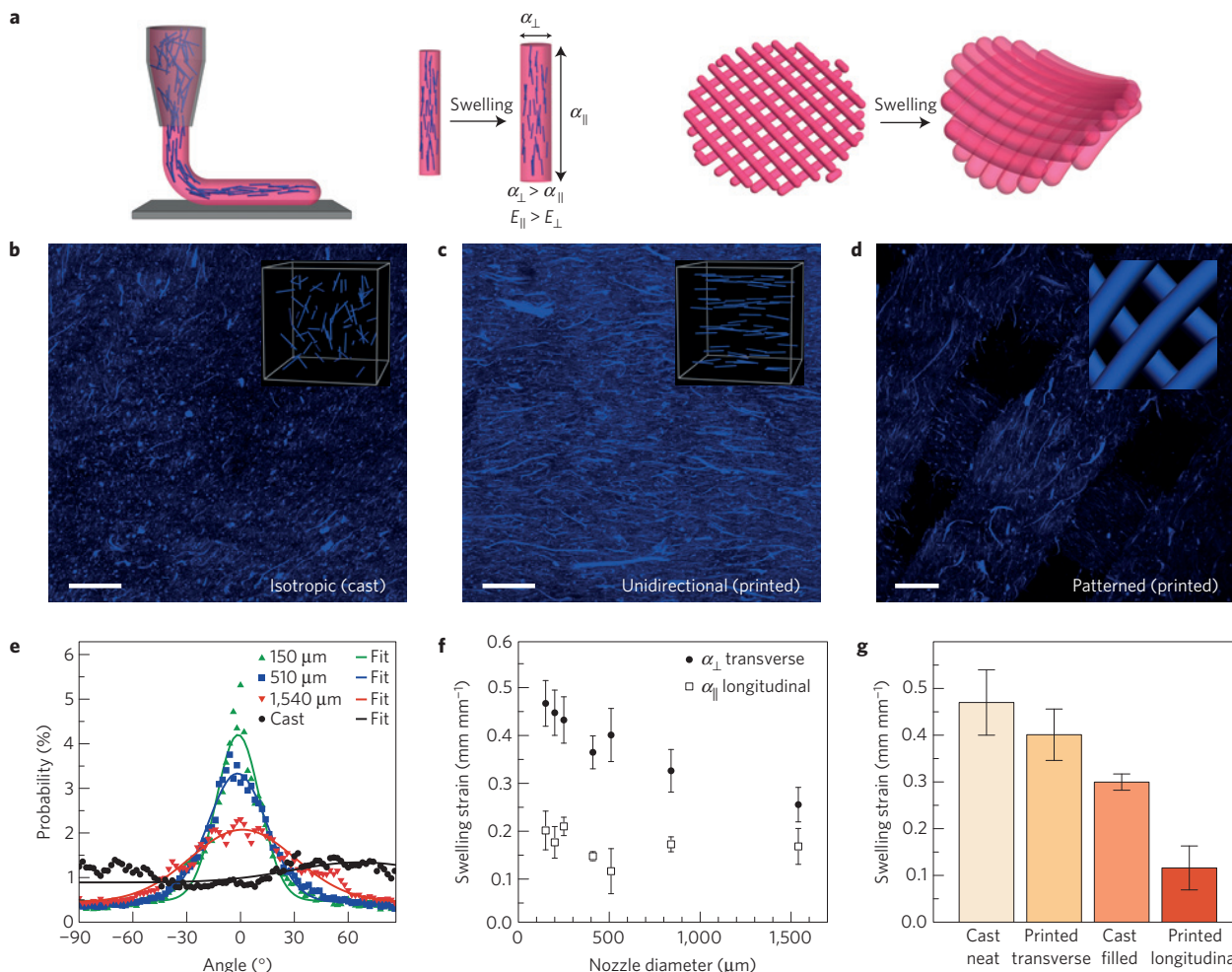
Figure 1 | Programming localized anisotropy via biomimetic 4D printing. One-step alignment of cellulose fibrils during hydrogel composite ink printing. **a**, Schematic of the shear-induced alignment of cellulose fibrils during direct ink writing and subsequent effects on anisotropic stiffness E and swelling strain α. **b**–**d**, Direct imaging of cellulose fibrils (stained blue) in isotropic (cast) (**b**), unidirectional (printed) (**c**) and patterned (printed) (**d**) samples (scale bar, 200 µm). **e**, Applying Fourier analysis to NFC-stained images allows quantification of directionality: printed unidirectional samples exhibit a clear peak at 0°, corresponding to the print direction, whereas isotropic samples show no clear directional peaks. **f**, Effect of nozzle diameter on transverse and longitudinal swelling behaviour of printed hydrogel composites. **g**, Swelling strain of cast and printed samples (nozzle diameter = 510 µm). All error bars represent the standard deviation ($n = 6$).

and curvature strain tensors, and traction along the midplane must be identical. Reflecting these conditions, we consider a theoretical model for a three-dimensional structure produced by a prescribed print path, where the print path dictates the local orientation of the cellulose fibrils. The bottom layer is printed parallel to the $\mathbf{e_x}$ direction, and the top layer has been rotated anticlockwise by θ degrees (see Supplementary Fig. 1).

The resulting curvatures depend on the elastic moduli, the swelling ratios, the ratio of layer thicknesses $m = a_{bottom}/a_{top}$ and total bilayer thickness $h = a_{top} + a_{bottom}$. The mean and Gaussian curvatures scale, respectively, as

$$H = c_1 \frac{\alpha_{\parallel} - \alpha_{\perp}}{h} \frac{\sin^2(\theta)}{c_2 - c_3 \cos(2\theta) + m^4 \cos(4\theta)}$$

and

$$K = -c_4 \frac{(\alpha_{\parallel} - \alpha_{\perp})^2}{h^2} \frac{\sin^2(\theta)}{c_5 - c_6 \cos(2\theta) + m^4 \cos(4\theta)}$$

where the c_i are functions of the elastic constants (which are given by their equilibrium swollen values) and m (see Supplementary Information for further details). In the limit that

$\theta \to 0°$, we recover the classical Timoshenko equation[26], whereas perpendicular layers ($\theta = 90°$) return a saddle-shaped structure[9].

A series of simple printed bilayer architectures allows us to explore these relationships and the quantitative connection between swelling as well as elastic anisotropy and the curvature of the target surface (Fig. 2). We first demonstrate independent control over both the mean and Gaussian curvatures, the two invariants associated with the curvature of any surface.

Positive Gaussian curvature can be generated by swelling a structure that is primarily made of concentric circles[27] (Fig. 2a). This structure is conical ($K \sim 0$) far away from the tip, but has Gaussian curvature $K \sim \epsilon^2/h^2$ concentrated near the apex, where $\epsilon \sim (\alpha_{\parallel} - \alpha_{\perp})$. The conical opening angle, both measured and calculated using our theory, is $\theta = 52°$ (see Supplementary Information). On the other hand, almost uniform negative Gaussian curvature associated with saddle-like shapes comes from an orthogonal bilayer lattice[9] (Fig. 2b). The orthogonal swelling of each layer yields a surface that is curved oppositely along two directions—that is, a saddle-shaped surface with mean curvature $H \sim 0$ and Gaussian curvature $K \sim -\epsilon^2/h^2$. Combining these two morphologies produces a sample with zones of both positive and negative Gaussian curvature (Fig. 2c). Simple structures that
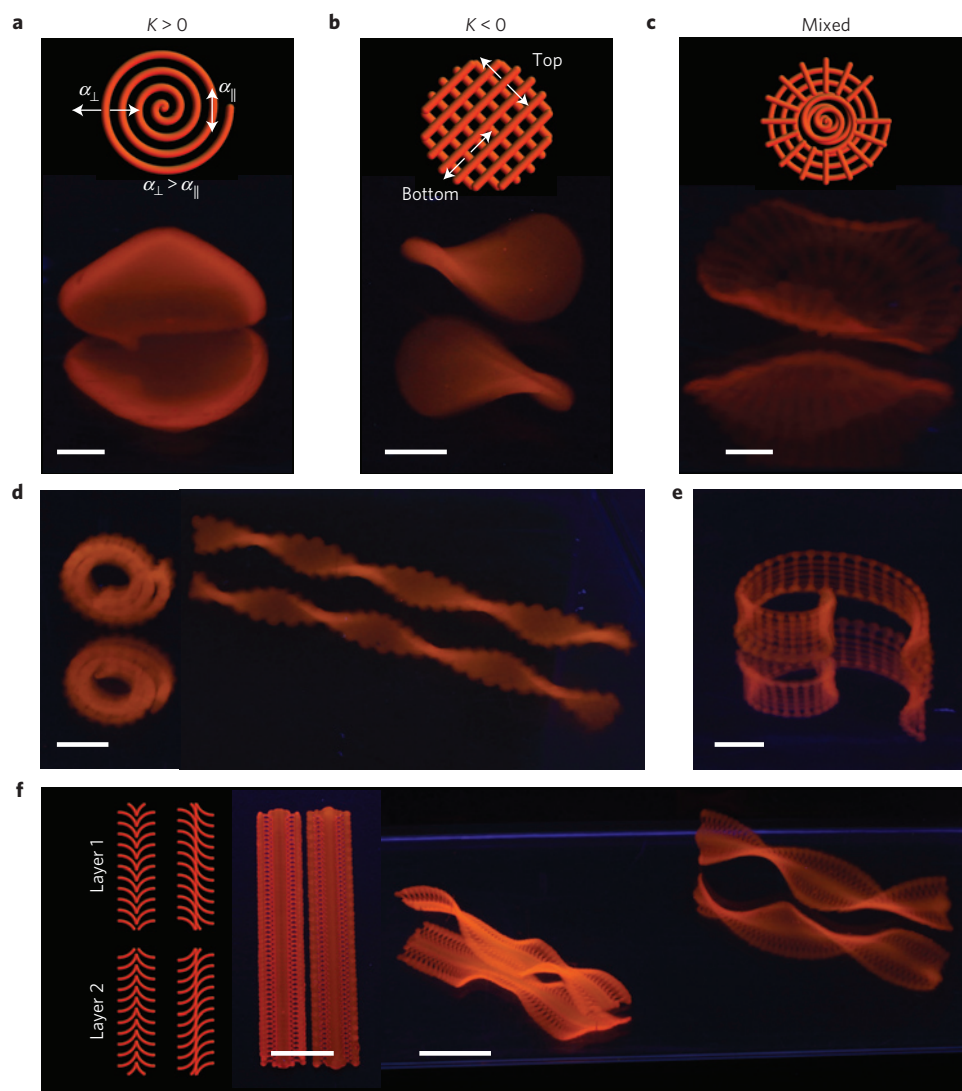
Figure 2 | Printing simple architectures with precise control over mean and Gaussian curvatures. a–c, Print paths and final swollen geometries display positive (**a**), negative (**b**) and varying Gaussian curvature (**c**) (scale bar, 2.5 mm). **d**, Bending and twisting conformations are possible with strips of 90°/0° (left) and −45°/45° (right) print path orientations (see text for details). **e**, A gradient in local interfilament spacing generates a logarithmic spiral (scale bars, 5 mm). **f**, Breaking lateral symmetry in print paths order takes a ruffled structure (left) to a helicoidal structure (right) (scale bar, 10 mm).

exhibit uniform cylindrical curvature ($H \neq 0, K = 0$) arise with 90°/0° orientation of ink paths, whereas −45°/45° yields twisted bilayer strips (Fig. 2d), similar to their natural counterparts the *Erodium* awn[28] and the *Bauhinia* seed pod[9], respectively. Because interfilament spacing acts as a proxy for the thickness (see Supplementary Text), we can also make the curvature spatially inhomogeneous, leading, for example, to the logarithmic spiral (Fig. 2e and more examples in Supplementary Figs 7 and 8). Overlapping circular arcs generate a structure, which transitions from primarily swelling perpendicular to the spine of the petal to parallel to the border, leading to a surface with varying K (Fig. 2f). This structure possesses negative Gaussian curvature, which increases towards the edge. Similarly, in the print path of a ribbon, breaking translational symmetry across the midplane and replacing it by reflection symmetry yields a ruffled structure, whereas breaking the reflection symmetry across the midplane and the midline yields a helicoid[29,30] (Fig. 2f and Supplementary Movie 1). Figure 2 also illustrates our ability to control curvatures of both solid (infilled) structures and lattice-based structures with varying porosity (see Supplementary Text for details).

By combining patterns that generate simple curved surfaces, we created a series of functional folding flower architectures to demonstrate the capabilities of bio-4DP (Fig. 3). Inspired by flower opening/closing[31], we printed petals in a floral form (Fig. 3a) comprised of a bilayer lattice with a 90°/0° configuration, similar to previous bilayer strips[9,16] and see that the structure closes as it swells (see Supplementary Movie 2). As a control, we also printed an identical pattern using an ink devoid of microfibrils, and observe that it remains flat on swelling (Supplementary Fig. 9). When the petals are printed with the ink filaments oriented at −45°/45° (Fig. 3b) the resulting structure yields a twisted configuration (see Supplementary Movie 3)[9]; the chirality of the resulting structures is due to broken top–bottom symmetry of the bilayer and thence differential swelling across the thickness. Importantly, these constructs contain spanning filaments that are readily fabricated by direct writing of the viscoelastic composite ink. The interfilament spacing promotes rapid uptake of water through the filament radius (∼100 μm), leading to shape transformations that occur on the order of minutes (Fig. 3a,b), consistent with diffusion-limited dynamics (Supplementary Fig. 10). Whereas the shape transformation shown in Fig. 3 is not reversible, replacing

Figure 3 | Complex flower morphologies generated by biomimetic 4D printing. a,b, Simple flowers composed of 90°/0° (**a**) and −45°/45° (**b**) bilayers oriented with respect to the long axis of each petal, with time-lapse sequences of the flowers during the swelling process (bottom panel) (scale bars, 5 mm, inset = 2.5 mm). **c–f**, Print path (**c**), printed structure (**d**) and resulting swollen structure (**e**) of a flower demonstrating a range of morphologies inspired by a native orchid, the *Dendrobium helix* (courtesy of Ricardo Valentin) (**f**). Based on the print path, this orchid architecture exhibits four different configurations: bending, twisting and ruffling corolla surrounding the central funnel-like domain (scale bars, 5 mm).

the poly(*N*,*N*-dimethylacrylamide) matrix with stimuli-responsive poly(*N*-isopropylacrylamide) allows reversible shape changes in water of varying temperature (Supplementary Fig. 11 and Supplementary Movie 4).

As an example of the versatility of bio-4DP, we mimic the complexity of the orchid *Dendrobium helix* by encoding multiple shape-changing domains. The print path is designed with discrete bilayer orientations in each petal (Fig. 3c,d, see Supplementary Movie 5 for a video of the printing process, and Supplementary Fig. 12 for the fibril alignment needed for these complex shapes). The resulting 3D morphology (Fig. 3e and Supplementary Movie 6) following swelling in water resembles the orchid (Fig. 3f) and exhibits four distinct types of shape change (three different petal types and the flower centre), based on configurations demonstrated in Figs 2 and 3a,b.

In each of the previous examples, our model can be used to predict the final curvature based on the print path, which naturally suggests the inverse problem: how may we design print paths associated with specific target surfaces? In an illustrative demonstration, we harness continuous, detailed control over print path, predicted by our model and enabled by bio-4DP, to mimic the complex curvature of the calla lily flower (*Zantedeschia aethiopica*, Fig. 4a). Our model enables the translation of a complex three-dimensional surface (Fig. 4b and Supplementary Text) into the two-layered print path (Fig. 4d and Supplementary Movie 7) required to achieve this shape using only the local curvatures (Fig. 4c), swelling ratio, elastic constants, height and size of the structure. Gauss's Theorema Egregium dictates the metric of one of the layers (as demonstrated in ref. 25) whereas our mechanical model determines the architecture of the other layer. The good agreement between the final 3D shape, calculated theoretically (Fig. 4e) and printed experimentally (Fig. 4f), illustrates our unprecedented control over smooth gradients in curvature and the consequent ability to create shapes that are almost impossible to create by any other method. In addition, our bio-4DP approach allows the fabrication of shape changing elements beyond planar bilayers, by encoding anisotropy in the *z*-direction (Supplementary Fig. 13).

Our 4D printing method relies on a combination of materials and geometry that can be controlled in space and time. This technique has potential as a platform technology, where the hydrogel composite ink design can be extended to a broad
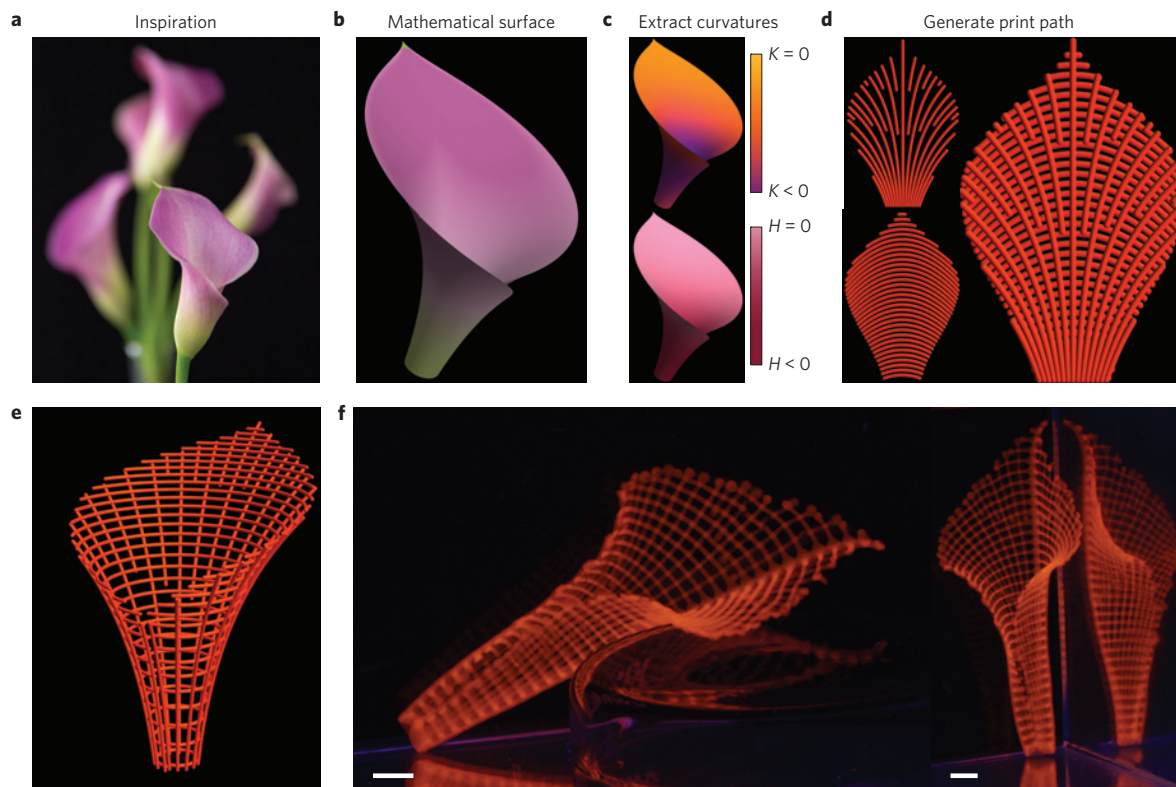
Figure 4 | Predictive 4D printing of biomimetic architectures. a–d, A native calla lily flower (**a**) inspires the mathematically generated model of the flower (**b**), with a well-defined curvature (**c**), that leads to the print path (**d**) obtained from the curvature model to create the geometry of the flower on swelling (see text and Supplementary Information). **e,f**, After swelling, the transformed calla lily (**f**) exhibits the same gradients of curvature as the predicted model (**e**), nozzle size = 410 μm (scale bars, 5 mm).

range of matrices (for example, liquid-crystal elastomers) and anisotropic fillers (for example, metallic nanorods) that when combined with flow-induced anisotropy allows us to produce dynamically reconfigurable materials with tunable functionality. Through the control of printing parameters, such as filament size, orientation, and interfilament spacing, we can create mesoscale bilayer architectures with programmable anisotropy that morph into given target shapes, predicted by our model, on immersion in water. All together, owing to our biocompatible and flexible ink design, our study opens new avenues for creating designer shape-shifting architectures for tissue engineering, biomedical devices, soft robotics and beyond.

Methods

Methods and any associated references are available in the online version of the paper.

References

1. Hu, J., Meng, H., Li, G. & Ibekwe, S. I. A review of stimuli-responsive polymers for smart textile applications. *Smart Mater. Struct.* **21**, 053001 (2012).
2. Felton, S., Tolley, M., Demaine, E., Rus, D. & Wood, R. A method for building self-folding machines. *Science* **345**, 644–646 (2014).
3. Randall, C. L., Gultepe, E. & Gracias, D. H. Self-folding devices and materials for biomedical applications. *Trends Biotechnol.* **30**, 138–146 (2012).
4. Fernandes, R. & Gracias, D. H. Self-folding polymeric containers for encapsulation and delivery of drugs. *Adv. Drug Deliv. Rev.* **64**, 1579–1589 (2012).
5. Kuribayashi-Shigetomi, K., Onoe, H. & Takeuchi, S. Cell origami: self-folding of three-dimensional cell-laden microstructures driven by cell traction force. *PLoS ONE* **7**, e51085 (2012).
6. Forterre, Y., Skotheim, J., Dumais, J. & Mahadevan, L. How the Venus flytrap snaps. *Nature* **433**, 421–425 (2005).
7. Awell, B. J., Kriedemann, P. E. & Turnbull, C. G. N. *Plants in Action* (Macmillan Education AU, 1999).
8. Reyssat, E. & Mahadevan, L. Hygromorphs: from pine cones to biomimetic bilayers. *J. R. Soc. Interface* **6**, 951–957 (2009).
9. Armon, S., Efrati, E., Kupferman, R. & Sharon, E. Geometry and mechanics in the opening of chiral seed pods. *Science* **333**, 1726–1730 (2011).
10. Fratzl, P. & Burgert, I. Actuation systems in plants as prototypes for bioinspired devices. *Phil. Trans. R. Soc. A* **6**, 1541–1557 (2009).
11. Ge, Q., Qi, H. J. & Dunn, M. L. Active materials by four-dimension printing. *Appl. Phys. Lett.* **103**, 131901 (2013).
12. Ratna, D. & Karger-Kocsis, J. Recent advances in shape memory polymers and composites: a review. *J. Mater. Sci.* **43**, 254–260 (2008).
13. Erb, R. M., Sander, J. S., Grisch, R. & Studart, A. E. R. Self-shaping composites with programmable bioinspired microstructures. *Nature Commun.* **4**, 1712 (2012).
14. Thérien-Aubin, H., Wu, Z. L., Nie, Z. & Kumacheva, E. Multiple shape transformations of composite hydrogel sheets. *J. Am. Chem. Soc.* **125**, 4834–4839 (2013).
15. Tibbits, S. 4D printing: multi-material shape change. *Archit. Des.* **84**, 116–121 (2014).
16. Ionov, L. Bioinspired microorigami by self-folding polymer films. *Macromol. Chem. Phys.* **214**, 1178–1183 (2012).
17. Na, J. H. *et al*. Programming reversibly self-folding origami with micropatterned photo-crosslinkable polymer trilayers. *Adv. Mat.* **27**, 79–85 (2015).
18. Liu, Y., Boyles, J. K., Genzer, J. & Dickey, M. D. Self-folding of polymer sheets using local light absorption. *Soft Matter* **8**, 1764–1769 (2012).
19. Lewis, J. A. Direct ink writing of 3D functional materials. *Adv. Funct. Mater.* **16**, 2193–2204 (2006).
20. Oytun, F., Kahveci, M. U. & Yagci, Y. Sugar overcomes oxygen inhibition in photoinitiated free radical polymerization. *J. Polym. Sci. A* **51**, 1685–1689 (2013).
21. Josset, S. *et al*. Energy consumption of the nanofibrillation of bleached pulp, wheat straw and recycled newspaper through a grinding process. *Nord. Pulp Paper Res. J.* **29**, 167–175 (2014).

22. Haraguchi, K. & Takehisa, T. Nanocomposite hydrogels: a unique organic-inorganic network structure with extraordinary mechanical, optical, and swelling/de-swelling properties. *Adv. Mater.* **14,** 1120–1124 (2002).
23. Compton, B. G. & Lewis, J. A. 3D-printing of lightweight cellular composites. *Adv. Mater.* **26,** 5930–5935 (2014).
24. Smay, J. E., Cesarano, J. & Lewis, J. A. Colloidal inks for directed assembly of 3-D periodic structures. *Langmuir* **18,** 5429–5437 (2002).
25. Aharoni, H., Sharon, E. & Kupferman, R. Geometry of thin nematic elastomer sheets. *Phys. Rev. Lett.* **113,** 257801 (2014).
26. Timoshenko, S. Analysis of bi-metal thermostats. *J. Opt. Soc. Am.* **11,** 233–255 (1925).
27. Modes, C. D., Bhattacharya, K. & Warner, M. Gaussian curvature from flat elastic sheets. *Proc. R. Soc. A* **467,** 1121–1140 (2011).
28. Abraham, Y. *et al*. Tilted cellulose arrangement as a novel mechanism for hygroscopic coiling in the stork's bill awn. *J. R. Soc. Interface* **9,** 640–647 (2012).
29. Liang, H. & Mahadevan, L. The shape of a long leaf. *Proc. Natl Acad. Sci. USA* **106,** 22049–22054 (2009).
30. Liang, H. & Mahadevan, L. Growth, geometry, and mechanics of a blooming lily. *Proc. Natl Acad. Sci. USA* **108,** 5516–5521 (2011).
31. van Doorn, W. G. Flower opening and closure: a review. *J. Exp. Bot.* **54,** 1801–1812 (2003).

Author contributions

A.S.G., R.G.N. and J.A.L. developed the 4D printing concept. A.S.G. designed the ink composition, printed and prepared all samples, obtained photographic images, and characterized alignment, swelling, mechanical and rheological properties. E.A.M. and L.M. developed the theoretical model. E.A.M. rendered and calculated the desired shapes and print paths, and generated the G-code for printing. A.S.G., E.A.M., L.M. and J.A.L. wrote the manuscript. A.S.G. and E.A.M. developed the figures. All authors commented on the manuscript.

Additional information

Supplementary information is available in the online version of the paper. Reprints and permissions information is available online at www.nature.com/reprints. Correspondence and requests for materials should be addressed to L.M. or J.A.L.

Competing financial interests

The authors declare no competing financial interests.

Methods

The general procedure for creating 4D printed architectures involves the preparation of ink containing clay, monomer, NFC, photoinitiator, enzyme/glucose and deionized water. Architectures are printed at room temperature in air, and ultraviolet cured after print completion. Samples are immersed in deionized water to allow swelling and shape transformation.

Ink preparation and details. Synthetic hectorite clay, Laponite XLG (Southern Clay Products), is added, enabling polymerization to initiate from the surface on the clay due to the high cationic exchange capacity of the clay[32]. The clay forms a strong physical, multifunctional crosslinker, with recent modelling suggesting that an increase in clay content results in an increase in inter-particle crosslinking polymer chains[33]. The network gel formed by the process imparts high stretchability and strength compared to covalently crosslinked hydrogels without clay[22]. As higher clay concentrations result in higher crosslink densities, and lower swelling, we sought a minimal clay concentration. Thus, ~10 wt% clay was chosen as the minimum clay concentration needed for printed filaments to flow and retain shape as desired. Our source for nanofibrillated cellulose (NFC) is unbleached and processed directly from soft wood pulp (*Picea abies* and *Pinus* spp.), graciously donated by the Applied Wood Material Lab at EMPA. The maximum NFC concentration that allowed for smooth, clog-free print behaviour was ~0.8 wt%, and thus was chosen for all experiments. The monomer used in this gel is *N*,*N*-dimethylacrylamide or *N*-isopropylacrylamide, which forms a biocompatible hydrogel capable of significant swelling in water, both of which have been shown to utilize the aforementioned clay-crosslinking system[34].

Oxygen inhibition (OI) is a major limitation in 3D printing polymer inks undergoing free-radical polymerization. OI can lead to hundreds of micrometres or more of poorly cured surface gel. With 3D printed features of this same scale, it is a major hurdle to overcome. To prevent OI we report the use of a naturally occurring oxygen-scavenging enzyme, glucose oxidase, which has recently been demonstrated to improve ambient ultraviolet polymerization in aqueous hydrogels[20]. We report the use of glucose oxidase/glucose for the first time in 3D printed hydrogel inks, an essential addition for successful polymerization in ambient conditions; without the enzyme, 200 μm printed features are unable to be cured in ambient conditions, whereas the addition of the glucose oxidase enables cured architectures with no detectable OI.

NFC is diluted from a stock solution to deoxygenated water under nitrogen flow, and mixed thoroughly using a Thinky mixer (ARE-310, Thinky) in a closed container. Laponite XLG clay is then added under nitrogen flow and mixed again using the Thinky mixer. Monomer, *N*,*N*-dimethylacrylamide (DMAm) or *N*-isopropylacrylamide (NIPAm) (Sigma Aldrich, unmodified), is added to this NFC-clay solution under nitrogen flow and mixed again using the Thinky mixer. Irgacure 2959 (BASF) is added as the ultraviolet photoinitiator. D-(+)-glucose (Sigma Aldrich) and glucose oxidase (from *Aspergillus niger*, Sigma Aldrich) are added as oxygen scavengers. Under nitrogen flow the ink is hand mixed, followed by mixing using the Thinky mixer. The final concentrations of each component are as follows: 77.6% deionized water, 0.73% NFC, 9.7% Laponite XLG clay, 7.8% monomer, 0.097% Irgacure 2959, 0.23% glucose oxidase, 3.8% glucose. Finally 1 vol% of a 5 mg ml⁻¹ solution of a monomeric rhodamine dye (PolyFluor 570-methacryloxyethyl thiocarbonyl rhodamine B, Polysciences) is added under nitrogen flow and mixed using the Thinky mixer. Under nitrogen flow the ink is loaded into a syringe barrel and centrifuged to remove bubbles. The ink is then mounted to the printer and attached to a controlled air pressure input (Nordson EFD). Via Luer-lock connection a variety of commercial nozzles of varying diameter (Nordson EFD) can be attached. All nozzles were stainless steel, straight tips, with 10 mm nozzle lengths.

Printing procedure. Print paths were generated via production of G-code which outputs the XYZ motion of the 3D printer (ABG 10000, Aerotech). G-code was generated either by hand, using MeCode Python scripting (Jack Minardi (Voxel8),

Daniel Fitzgerald (WPI)), or by scripting in Mathematica. Samples were printed on glass slides covered with a Teflon adhesive film (Bytac, Saint-Gobain) and cured for 200 s using an Omnicure ultraviolet source (Series 2000, Lumen Dynamics). After curing, the printed architecture is coated in a thin film of DI water to remove it from the substrate. The sample was then immersed in DI water to allow swelling and shape change.

Characterizing alignment and swelling. To test NFC alignment we printed unidirectional, solid-infilled samples with various sizes of nozzles (150–1,500 μm diameter). We also fabricated NFC filled and unfilled cast hydrogel samples for comparison. Longitudinal (print direction) and transverse strains were calculated by measuring sample dimensions as fabricated and after reaching equilibrium swelling in DI water, or approximately five days. These samples were then stained via immersion in 5 ml of a 0.1 mg ml⁻¹ solution of Calcofluor White (Sigma Aldrich), with 200 μl of 10 wt% potassium hydroxide solution added, for 24 h. They were removed from the staining solution and soaked in DI water for 24 h, and then imaged via confocal microscopy (LSM710, Zeiss). Z slices of approximately 10 μm were acquired and stacked into maximum projection images using ImageJ. To quantify alignment, the ImageJ plugin Directionality (creator: J. Yvez-Tinevez), was applied to the unmodified maximum projection images, resulting in a histogram of relative alignment in different orientations. A Gaussian fit is applied to the resulting histograms.

Mechanical testing. Tensile specimens were prepared via printing and curing. The print path of transverse and longitudinal orientations are shown in Supplementary Fig. 5. Samples were tested either immediately after fabrication or after soaking in DI water for five days. The samples were tested on an Instron mechanical testing machine (Model 3342) with a 10 N load cell at a rate of 100 mm min⁻¹ until failure. Stress and strain were calculated via initial specimen dimensions. Moduli were calculated from linear regions of the stress–strain curves.

Rheological characterization. Inks rheology was characterized via testing on a rheometer (DHR-3, TA Instruments) with a 40 mm diameter, 2.005° cone-plate geometry. Flow experiments were conducted via a logarithmic sweep of shear rates (0.1–10,001 s⁻¹). Oscillation experiments were conducted via a fixed frequency of 1 Hz and oscillatory strain of 0.01, with a sweep of stress (0.1–3,000 Pa). All experiments were performed in ambient conditions with a gap height of 56 μm and preliminary soak time of 60 s.

Macro imaging. All photographic images were taken under a broad spectrum ultraviolet light source to excite the rhodamine dye in the ink. Images were taken with DSLR cameras (Mark III or Rebel T3i, Canon) with a variety of lenses. As-printed specimens were photographed in ambient conditions, while resulting shape transformations were captured in an acrylic enclosure containing deionized water.

Code availability. G-code (print path) for all structures printed in Figs 2–4 is available on request.

References

32. Haraguchi, K., Li, H.-J., Matsuda, K., Takehisa, T. & Elliott, E. Mechanism of forming organic/inorganic network structures during *in-situ* free-radical polymerization in PNIPA-clay nanocomposite hydrogels. *Macromolecules* **38**, 3482–3490 (2005).
33. Yong, X., Kuksenok, O. & Balazs, A. C. Modeling free radical polymerization using dissipative particle dynamics. *Polymer* **72**, 217–225 (2015).
34. Haraguchi, K., Murata, K. & Takehisa, T. Stimuli-responsive nanocomposite gels and soft nanocomposites consisting of inorganic clays and copolymers with different chemical affinities. *Macromolecules* **45**, 385–391 (2012).

Biomimetic 4D printing

A. Sydney Gladman[a,b,1], Elisabetta A. Matsumoto[a,b,1], Ralph
G. Nuzzo[c], L. Mahadevan[a,b,d], and Jennifer A. Lewis[a,b]

[a]*John A. Paulson School of Engineering and Applied Sciences,*

*Harvard University, 29 Oxford Street, Cambridge, MA 02138*

[b]*Wyss Institute for Biologically Inspired Engineering,*

Harvard University, 60 Oxford Street, Cambridge, MA 02138

[c]*School of Chemical Sciences, University of Illinois Urbana-Champaign, Urbana, IL 61801*

[d]*Departments of Physics and Organismic and Evolutionary Biology,*

and Kavli Institute for NanoBio Science and Technology,

Harvard University, 29 Oxford Street, Cambridge, MA 02138 and

[1]*These authors contributed equally.*

A.   Forward problem: finding curvatures of the target surface given print paths, and bilayer anisotropy, interfilament spacing
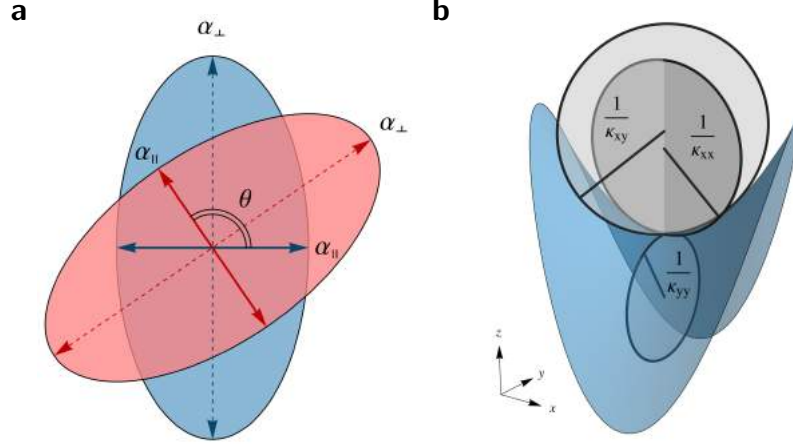
Supplementary Figure 1 | a, Schematic of the printed bilayer geometry used in the model. The first and second layers have filaments aligned along the $\mathbf{e_x}$ and $\cos(\theta)\mathbf{e_x} + \sin(\theta)\mathbf{e_y}$ directions, respectively. **b,** The curvature tensor κ has two invariants mean $H = \frac{1}{2}(\kappa_{xx} + \kappa_{yy})$ and Gaussian $K = \kappa_{xx}\kappa_{yy} - \kappa_{xy}^2$ curvature.

We have generalised the classical Timoshenko theory for bimetallic strips to account for the anisotropy of the ink, as well as the intrinsically two-dimensional patterning enabled by our printing method. Motivated by the theory of laminated composites, our model considers a bilayer patch of total height h of hydrogel composite ink that swells anisotropically because the cellulose fibril alignment affects the elastic moduli and therefore the swelling strain tensor, $\varepsilon^{\mathrm{s}} = \begin{bmatrix} \alpha_{\parallel} & 0 \\ 0 & \alpha_{\perp} \end{bmatrix}$, [34, 35]. The ink may be treated as an orthotropic elastic material, which satisfies the stress-strain relationship $\sigma_{ij} = E_{ijkl}\varepsilon^{\mathrm{e}}_{kl}$, (throughout the standard Einstein summation convention is $a_i b_{ij} = \sum_{i=1}^{2} a_i b_{ij}$), where the total strain tensor $\varepsilon = \varepsilon^{\mathrm{e}} + \varepsilon^{\mathrm{s}}$ is the sum of the elastic ε^{e} and swelling ε^{s} strain tensors, and the only non-zero components of the elastic moduli tensor E_{ijkl} are $E_{xxxx} = E_{\parallel}$, $E_{yyyy} = E_{\perp}$ and $E_{xyxy} = E_{\times}$. Without loss of generality, we take the print path of the first layer to be along $\mathbf{e_x}$ and the second

layer to be in the $\cos(\theta)\mathbf{e_x} + \sin(\theta)\mathbf{e_y}$, direction. The elastic moduli and strain tensors of the second layer transform according to $E_{mnpq}(\theta) = r_{im}(\theta)r_{jn}^{-1}(\theta)r_{kp}(\theta)r_{lq}^{-1}(\theta)E_{ijkl}$ and $\varepsilon_{ij}(\theta) = r_{ik}(\theta)r^{-1}(\theta)_{jl}\varepsilon_{kl}$, where $r_{ij}(\theta)$ and $r_{ij}^{-1}(\theta) = r_{ji}$ are components of the rotation matrix and its inverse (transpose), respectively, with $r_{ij}r_{kj} = \delta_{ik}$.

For small deflections, the strain tensor in a thin film is given by $\varepsilon_{ij} = -z\kappa_{ij}$, where z is the distance from the interface and κ_{ij} are components of the curvature tensor [36]. At the boundary between layers, the displacements and tractions are continuous. In the unidirectional strain case, these boundary conditions are commonly solved by the introduction of a neutral surface, a location where all of the forces and torques balance. However, for anisotropic materials, this notion is ill defined. Each layer is subject to displacement coming from the swelling, $u^{\mathrm{s}}(x,y) = \int dA\varepsilon_{ij}^{\mathrm{s}}$, which must be balanced by displacements due to curvature. The stress tensor is related to the curvature through the bending moments $M_{ij} = \int dz z\sigma_{ij} = \int dz z E_{ijkl}\varepsilon_{kl}^{\mathrm{e}}$. Combining these, the equilibrium condition is given by:

$$\int dA \left[\varepsilon_{ij}^{\mathrm{s},(1)} + \frac{1}{a_1}E_{ijkl}^{-1}(0)M_{kl}\right] = \int dA \left[r_{ik}(\theta)r_{jl}^{-1}(\theta)\varepsilon_{kl}^{\mathrm{s},(2)} + \frac{1}{a_2}E_{ijmn}^{-1}(\theta)M_{mn}\right], \qquad (1)$$

where $M_{ij} = \int_{-a_1}^{0} E_{ijkl}(0)\kappa_{kl}z^2dz + \int_0^{a_2} E_{ijkl}(\theta)\kappa_{kl}z^2dz$ are the bending moments per unit length and a_1 and a_2 are the layer thicknesses. Given $\varepsilon^{\mathrm{s}(1)}$ and $\varepsilon^{\mathrm{s}(2)}$ solutions to the system of equations 1 yield the curvature tensor for the resulting swollen structure, and constitutes the forward problem. In the limit of unidirectional swelling, $\theta = 0$ and $\alpha_\perp = 0$, the classical Timoshenko result is recovered [26].

Given the swelling strains $\alpha_\parallel$ and $\alpha_\perp$ and elastic modulus tensor E, the system of Eqs. (1) can be solved for the for the curvature tensor, κ. We then obtain relations for the mean

curvature, $H = \frac{1}{2}\text{Tr}\kappa$, and Gaussian curvature, $K = \det\kappa$,

$$
\begin{aligned}
H &= \tfrac{1}{2}\text{Tr}(\kappa) = \frac{\alpha_\parallel - \alpha_\perp}{2h}\left(\frac{a_{xy}(c_0 b_{xx} - b_0 c_{xx}) + a_{xx}(b_0 c_{xy} - c_0 b_{xy}) + a_0(b_{xy}c_{xx} - b_{xx}c_{xy})}{a_{yy}(b_{xx}c_{xy} - b_{xy}c_{xx}) + a_{xy}(b_{yy}c_{xx} - b_{xx}c_{yy}) + a_{xx}(b_{xy}c_{yy} - b_{yy}c_{xy})}\right. \\
&\quad \left. + \frac{a_{yy}(c_0 b_{xy} - b_0 c_{xy}) + a_{xy}(b_0 c_{yy} - c_0 b_{yy}) + a_0(b_{yy}c_{xy} - b_{xy}c_{yy})}{a_{yy}(b_{xx}c_{xy} - b_{xy}c_{xx}) + a_{xy}(b_{yy}c_{xx} - b_{xx}c_{yy}) + a_{xx}(b_{xy}c_{yy} - b_{yy}c_{xy})}\right)
\end{aligned}
\tag{2}
$$

$$
\begin{aligned}
K &= \text{Det}(\kappa) = \frac{(\alpha_\parallel - \alpha_\perp)^2}{h^2}\frac{a_{xy}(c_0 b_{xx} - b_0 c_{xx}) + a_{xx}(b_0 c_{xy} - c_0 b_{xy}) + a_0(b_{xy}c_{xx} - b_{xx}c_{xy})}{a_{yy}(b_{xx}c_{xy} - b_{xy}c_{xx}) + a_{xy}(b_{yy}c_{xx} - b_{xx}c_{yy}) + a_{xx}(b_{xy}c_{yy} - b_{yy}c_{xy})} \\
&\quad \times \frac{a_{yy}(c_0 b_{xy} - b_0 c_{xy}) + a_{xy}(b_0 c_{yy} - c_0 b_{yy}) + a_0(b_{yy}c_{xy} - b_{xy}c_{yy})}{a_{yy}(b_{xx}c_{xy} - b_{xy}c_{xx}) + a_{xy}(b_{yy}c_{xx} - b_{xx}c_{yy}) + a_{xx}(b_{xy}c_{yy} - b_{yy}c_{xy})} \\
&\quad - \frac{(\alpha_\parallel - \alpha_\perp)^2}{h^2}\left(\frac{a_{yy}(b_0 c_{xx} - c_0 b_{xx}) + a_{xx}(c_0 b_{yy} - b_0 c_{yy}) + a_0(b_{xx}c_{yy} - b_{yy}c_{xx})}{a_{yy}(b_{xx}c_{xy} - b_{xy}c_{xx}) + a_{xy}(b_{yy}c_{xx} - b_{xx}c_{yy}) + a_{xx}(b_{xy}c_{yy} - b_{yy}c_{xy})}\right)^2,
\end{aligned}
\tag{3}
$$

where the ratio and sum of the layer thicknesses are, respectively, $m = a_1/a_2$ and $a_1 + a_2 = h$ and the coefficients are given by

$$
a_0 = (\alpha_\parallel - \alpha_\perp)\sin^2(\theta), \quad b_0 = -(\alpha_\parallel - \alpha_\perp)\sin(\theta)\cos(\theta), \quad c_0 = -a_0
$$

$$
a_{xx} = \frac{\cos^4(\theta) + 2m(m(2m+3)+2)}{6m(m+1)^2} + \frac{\sin^4(\theta)\left(4\cot^2(\theta)E_\times + E_\perp\right)}{6m(m+1)^2 E_\parallel} + \frac{m^3\left(E_\parallel\left(4\sin^4(\theta)E_\times + \sin^2(2\theta)E_\perp\right) + 4\cos^4(\theta)E_\times E_\perp\right)}{24(m+1)^2 E_\times E_\perp}
$$

$$
b_{xx} = \frac{\sin(2\theta)\left(E_\parallel - E_\perp\right)}{48m(m+1)^2 E_\times} + \frac{h\sin(4\theta)\left(E_\parallel - 4E_\times + E_\perp\right)}{96m(m+1)^2 E_\times} + \frac{m^3\left(8\sin(\theta)\cos^3(\theta)E_\times E_\perp - E_\parallel\left(8\sin^3(\theta)\cos(\theta)E_\times + \sin(4\theta)E_\perp\right)\right)}{48(m+1)^2 E_\times E_\perp}
$$

$$
c_{xx} = \frac{\sin^2(2\theta)\left(E_\times\left((m^4+1)E_\parallel - 4E_\times\right) + E_\perp\left(m^4\left(E_\times - E_\parallel\right) + E_\times\right)\right)}{24m(m+1)^2 E_\times E_\perp}
$$

$$
a_{xy} = -\frac{m^4\sin(4\theta) - 4\sin(\theta)\cos^3(\theta)}{12m(m+1)^2} + \frac{E_\times\left(4m^4\sin(\theta)\cos^3(\theta) - \sin(4\theta)\right)}{6m(m+1)^2 E_\parallel} - \frac{2m^3\sin^3(\theta)\cos(\theta)E_\times}{3(m+1)^2 E_\perp} - \frac{\sin(2\theta)\sin^2(\theta)E_\perp}{6m(m+1)^2 E_\parallel}
$$

$$
b_{xy} = \frac{(m^4+1)\cos(4\theta) + m(m(m+2)(m+6)+8)+1}{12m(m+1)^2} + \frac{\sin^2(2\theta)\left(E_\parallel + E_\perp\right)\left(4m^4 E_\times^2 + E_\parallel E_\perp\right)}{24m(m+1)^2 E_\parallel E_\times E_\perp}
$$

$$
c_{xy} = \frac{\sin(2\theta)\left(m^4\cos(2\theta) - \cos^2(\theta)\right)}{6m(m+1)^2} + \frac{2m^3\sin^3(\theta)\cos(\theta)E_\times}{3(m+1)^2 E_\parallel} + \frac{E_\times\left(\sin(4\theta) - 4m^4\sin(\theta)\cos^3(\theta)\right) + 2\sin^3(\theta)\cos(\theta)E_\parallel}{6m(m+1)^2 E_\perp}
$$

$$
a_{yy} = \frac{(m^4+1)\sin^2(2\theta)}{24m(m+1)^2} + \frac{(m^4+1)\sin^2(2\theta)E_\perp}{24m(m+1)^2 E_\parallel} - \frac{E_\perp\left(m^4\sin^2(2\theta)E_\parallel - 2\sin^2(\theta)E_\times\right)}{24m(m+1)^2 E_\parallel E_\times}
$$

$$
b_{yy} = \frac{\sin(4\theta) - 4m^4\sin(\theta)\cos^3(\theta)}{24m(m+1)^2} + \frac{m^3\sin^2(\theta)\sin(2\theta)E_\perp}{12(m+1)^2 E_\parallel} + \frac{\sin(2\theta)\left(E_\perp\left(\left(2m^4-1\right)\cos(2\theta)-1\right) + 2\sin^2(\theta)E_\parallel\right)}{48m(m+1)^2 E_\times}
$$

$$
c_{yy} = \frac{(m^4+1)\cos^4(\theta) + 2m(m(2m+3)+2)}{6m(m+1)^2} + \frac{\sin^4(\theta)E_\parallel + \sin^2(2\theta)E_\times}{6m(m+1)^2 E_\perp} + \frac{m^3 E_\perp\left(\sin^2(2\theta)E_\parallel + 4\sin^4(\theta)E_\times\right)}{24(m+1)^2 E_\parallel E_\times}.
\tag{4}
$$

As this is a quasi-static theory, we need only consider the moduli and swelling ratios present in the final, fully hydrated state of the ink. Given the longitudinal and transverse Youngs moduli $E_\parallel \sim 40$ kPa and $E_\perp \sim 20$ kPa and the shear modulus $E_\times \sim \frac{1}{4}(E_\parallel + E_\perp)(1 - \nu) \sim 15$ kPa, where we assume the Poisson ratio $\nu = 0$, the mean and Gaussian curvatures scale respectively as $H = c_1\frac{\alpha_\parallel - \alpha_\perp}{h}\frac{\sin^2(\theta)}{c_2 - c_3\cos(2\theta) + m^4\cos(4\theta)}$ and

$$K = -c_4 \frac{(\alpha_{\parallel} - \alpha_{\perp})^2}{h^2} \frac{\sin^2(\theta)}{c_5 - c_6 \cos(2\theta) + m^4 \cos(4\theta)},$$ (see main text) where the c_i are given by

$$
\begin{aligned}
c_1 &= 144(m-1)m(m+1)^3 \left(m^2+1\right) \\
c_2 &= 32m^8 + 288m^7 + 944m^6 + 1824m^5 + 2275m^4 + 1824m^3 + 944m^2 + 288m + 32 \\
c_3 &= 4m \left(8m^6 + 12m^5 + 8m^4 + 9m^3 + 8m^2 + 12m + 8\right) \\
c_4 &= 1152m^2(m+1)^4 \\
c_5 &= 32m^8 + 288m^7 + 944m^6 + 1824m^5 + 2275m^4 + 1824m^3 + 944m^2 + 288m + 32 \\
c_6 &= 4m \left(8m^6 + 12m^5 + 8m^4 + 9m^3 + 8m^2 + 12m + 8\right).
\end{aligned}
$$

We note that although real elastomers have a finite Poisson ratio, $\nu \sim 0.3 - 0.5$, the choice $\nu = 0$, made here, allowed for analytic inversion of the aforementioned equations. This choice also eliminates the edge boundary layers that otherwise make the analysis significantly more complex. In practice, we do not believe this would qualitatively change the results, as the primary source of curvature results from the difference in principal swelling directions.

B. The effective thickness

The ratio of interlayer thicknesses is crucial to determining the sign and magnitude of the resulting curvature for these structures. As the print nozzle does not have a dynamically variable radius, we have invoked an effective thickness based on variable interfilament spacing to achieve local gradients in curvature. Since each layer contains a fixed volume of ink, the effective thickness is given by the volume of ink divided by the cross-sectional area. Our theory is consistent with the resulting porous structures, as the curvature is slowly varying on the the level of filament diameter and interfilament spacing. Therefore, such a continuum approximation remains valid.

C. Inverse problem: finding print paths for a given target surface

In equilibrium, given κ, E, and h, Eqs. (1) yield $\varepsilon^{s(1)}$ and $\varepsilon^{s(2)}$, solutions to the inverse problem. As an example of this, our model enables the translation of a complex three-dimensional surface (Fig. 4b) described by the equation

$$\mathbf{r} = \frac{1}{2}\left\{ e^{\frac{u/2}{1+u/8}}\cos(v), e^{\frac{u/2}{1+u/8}}\sin(v), \frac{2u}{1+u/8} + \frac{16}{3} \right\}, \tag{5}$$

with $u \in (-\frac{4}{3}, 10)$ and $v \in (-\pi, 2\pi)$, into the two-layered print path (Fig. 4c, SI Video 6) required to achieve this shape requiring only the local curvatures, swelling ratio and elastic constants.

D. Calla lily print path:

The curvatures of our calla lily surface, Eqn. (5), are given by

$$
\begin{aligned}
H &= -\frac{64}{\left(e^{\frac{8u}{u+8}} + 16\right)^2} \\
K &= -\frac{128e^{-\frac{4u}{u+8}}}{\left(e^{\frac{8u}{u+8}} + 16\right)^{3/2}}.
\end{aligned} \tag{6}
$$

Since the shape is cylindrically symmetric, the calla lily may be "unrolled" onto the plane, via the transform $v \to x/(2\pi)$, $z \to y$. With these as inputs, solving Eqns. (2,3) generates a thickness profile $m(x,y)$ (shown in Fig. S2c) and an angular fieldΔ $\theta(x,y)$.

The angular field generates a local orientational swelling of the sheet, thereby defining the local metric

$$g(x,y) = R[\theta_0(x,y)]\left(\begin{bmatrix} \alpha_\parallel & 0 \\ 0 & \alpha_\perp \end{bmatrix} + R[\Delta\theta(x,y)]\begin{bmatrix} \alpha_\parallel & 0 \\ 0 & \alpha_\perp \end{bmatrix} R^T[\Delta\theta(x,y)]\right) R^T[\theta_0(x,y)] \tag{7}$$

where $\theta_0(x,y)$ measures the rotation from $\mathbf{e}_x$ to the orientation of the filaments in the bot-

tom layer at point $\{x, y\}$. Gauss's Theorema Egregium states that the intrinsic (Gaussian) curvature is encoded entirely in the metric and its derivatives up to second order

$$
\begin{aligned}
4(EG - F^2)K \;=\; & E\left(\partial_y E \partial_y G - 2\partial_x F \partial_y G + (\partial_x G)^2\right) + G\left(\partial_x E \partial_x G - 2\partial_x E \partial_y F + (\partial_y E)^2\right) \\
& + F\left(\partial_x E \partial_y G - \partial_y E \partial_x G - 2\partial_y E \partial_y F + 4\partial_x F \partial_y F - 2\partial_x F \partial_x G\right) \\
& - 2(EG - F^2)\left(\partial_y^2 E - 2\partial_{xy}F + \partial_x^2 G\right),
\end{aligned}
\tag{8}
$$

where the components of the metric tensor are given by $E = g_{11}$, $F = g_{12} = g_{21}$ and $G = g_{22}$ [37]. In the case of the lily, where the surface is cylindrically symmetric, the $\Delta \theta$ is constant along $\mathbf{e}_x$, such that $\Delta\theta_x = \Delta\theta_{xx} = \Delta\theta_{xy} = 0$, and equation (8) simplifies to

$$
\begin{aligned}
K \;=\; & \left(\alpha_{\parallel} - \alpha_{\perp}\right)\left(-\left(-\alpha_{\perp}^2 + \cos(2\,\Delta\theta)\left(\alpha_{\parallel} - \alpha_{\perp}\right)^2 - 6\alpha_{\perp}\alpha_{\parallel} - \alpha_{\parallel}^2\right)\right. \\
& \times \left(2\cos(\,\Delta\theta)\left(-2\theta_x^2\cos(\Delta\theta + 2\theta) - 4\theta_x\theta_y\sin(\Delta\theta + 2\theta) - \theta_{xx}\sin(\Delta\theta + 2\theta)\right.\right. \\
& \left.+ 2\theta_{xy}\cos(\Delta\theta + 2\theta) + 2\theta_y^2\cos(\Delta\theta + 2\theta) + \theta_{yy}\sin(\Delta\theta + 2\theta)\right) + \Delta\theta_y\left(4\theta_y\cos(2(\Delta\theta + \theta))\right. \\
& \left.\left.- 4\theta_x\sin(2(\Delta\theta + \theta))\right) + 2\Delta\theta_y^2\cos(2(\Delta\theta + \theta)) + \Delta\,\theta_{yy}\sin(2(\Delta\theta + \theta))\right) \\
& + \left(\alpha_{\parallel} - \alpha_{\perp}\right)\left(\alpha_{\perp} + \cos(\,\Delta\theta)\cos(\,\Delta\theta + 2\theta)\left(\alpha_{\parallel} - \alpha_{\perp}\right) + \alpha_{\parallel}\right) \\
& \times \left(4\cos^2(\Delta\theta)\theta_x^2\sin^2(\Delta\theta + 2\theta) - 4\cos(\,\Delta\theta)\theta_x\cos(\Delta\theta + 2\theta)\left(\,\Delta\theta_y\sin(2(\Delta\theta + \theta))\right.\right. \\
& \left.\left.+ 2\cos(\Delta\theta)\theta_y\sin(\Delta\theta + 2\theta)\right) - \left(\Delta\theta_y\sin(2(\Delta\theta + \theta)) + 2\cos(\Delta\theta)\theta_y\sin(\Delta\theta + 2\theta)\right)^2\right) \\
& + \left(\alpha_{\parallel} - \alpha_{\perp}\right)\left(\alpha_{\perp} + \cos(\,\Delta\theta)\cos(\,\Delta\theta + 2\theta)\left(\alpha_{\perp} - \alpha_{\parallel}\right) + \alpha_{\parallel}\right) \\
& \times \left(-4\cos^2(\Delta\theta)\theta_x^2\sin^2(\Delta\theta + 2\theta) + 4\cos(\,\Delta\theta)\theta_x\sin(\Delta\theta + 2\theta)\left(\,\Delta\theta_y\cos(2(\Delta\theta + \theta))\right.\right. \\
& \left.\left.+ 2\cos(\Delta\theta)\theta_y\cos(\Delta\theta + 2\theta)\right) + \left(\Delta\theta_y\sin(2(\Delta\theta + \theta)) + 2\cos(\Delta\theta)\theta_y\sin(\Delta\theta + 2\theta)\right)^2\right) \\
& + \cos(\,\Delta\theta)\sin(\,\Delta\theta + 2\theta)\left(\alpha_{\parallel} - \alpha_{\perp}\right)^2\left(4\cos^2(\Delta\theta)\left(-\theta_x^2\sin(2(\Delta\theta + 2\theta)) + 4\theta_x\theta_y\cos^2(\Delta\theta + 2\theta)\right.\right. \\
& \left.+ \theta_y^2\sin(2(\Delta\theta + 2\theta))\right) + 4\cos(\,\Delta\theta)\Delta\theta_y\left(\theta_x(\cos(3\Delta\theta + 4\theta) + \cos(\,\Delta\theta)) + \theta_y\sin(3\Delta\theta + 4\theta)\right) \\
& \left.\left.+ \Delta\theta_y^2\sin(4(\Delta\theta + \theta))\right)\right) \Big/ \left(\tfrac{1}{2}\left(\alpha_{\parallel}^2 + 6\alpha_{\parallel}\alpha_{\perp} + \alpha_{\perp}^2 - \left(\alpha_{\parallel} - \alpha_{\perp}\right)^2\cos(2\Delta\theta)\right)\right).
\end{aligned}
\tag{9}
$$

Using the method outlined by Aharoni, *et al* in Ref. [25], we calculate an initial line field $\theta_1(x, y)$ which dictates the geometry of the first layer.

Using interfilament spacing as a proxy for thickness h, we integrate streamlines of the θ
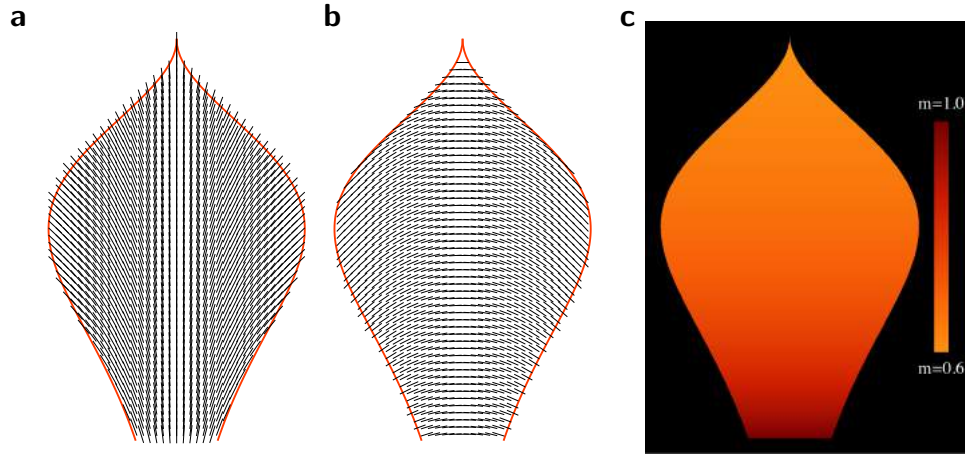
Supplementary Figure 2 | a,b, The orientational line fields, $\theta_0(x,y)$, for the bottom layer (**a**) and the top layer $\theta_1(x,y)$ (**b**). **c,** Height field, given in terms of the ratio of layer thicknesses $m = a_2/a_1$, for the lily. Darker colours indicate layers of approximately equal thickness, while lighter colours coincide with thinner bottom layer.

field to generate the print path for the first layer. The print path for the second layer is then obtained by adding the two fields $\theta_0(x,y) + \Delta\theta(x,y) = \theta_1(x,y)$. The print paths for the lily are shown in Fig. 4c. Due to the symmetries of the lily, streamlines of the second layer (corresponding to $\theta_1(x,y)$) were integrated first, starting with points equally spaced along the spine of the petal. The streamlines for the bottom layer were created with an iterative process. The first set of lines were integrated from points along the bottom ($y = 0$) of the lily, separated by the same spacing as the top layer. The second set were started at intermediate spacing between the first points, but line segments were deleted if they were closer than the inverse of the thickness. This process was repeated until no additional line segments could be added to the domain of the lily.

[34] Leknitskii, S. G. *Anisotropic Plates.* (Gordon Breach, 1968).

[35] Reddy, J. N. *Mechanics of Laminated Composite Plates and Shells, 2nd edn.* (CRC Press, Boca Raton, 2004).

[36] Mansfield, E. H. *The Bending & Stretching of Plates.* (Cambridge University Press, Cambridge, 1989).

[37] Gauss, K. F. *General Investigations of Curved Surfaces of 1827 and 1825.* (trans. Morehead, J. C. & Hiltebeitel, A. M. (The Princeton University Library, Princeton, 1902).
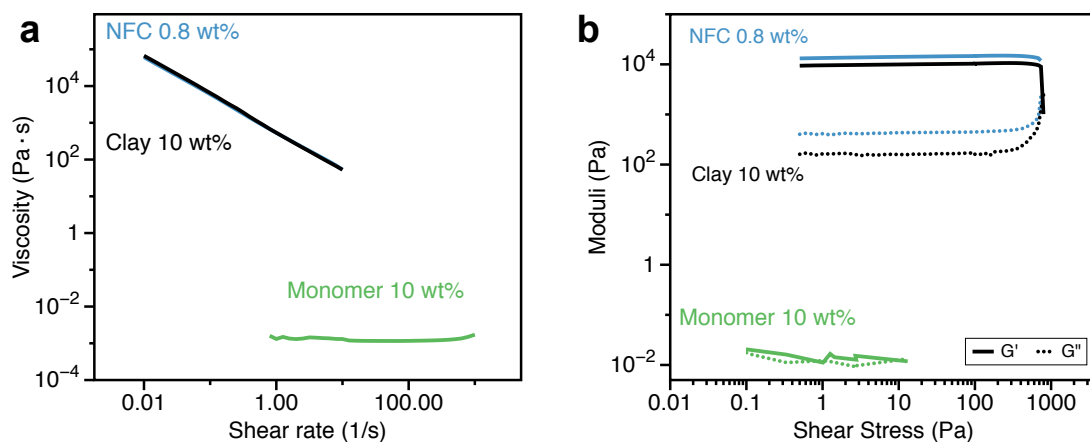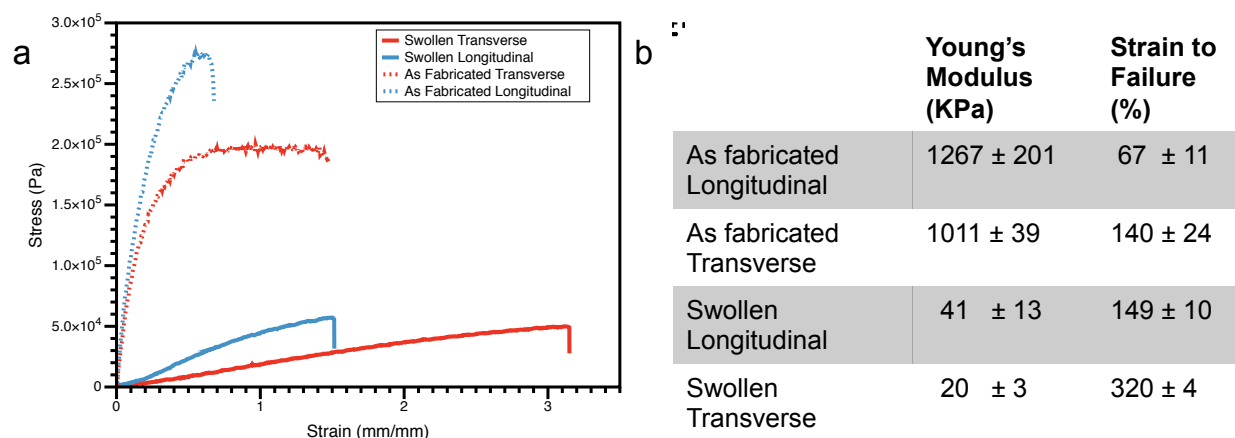
Supplementary Figure 3 | Log-log plots of (**a**) ink viscosity as a function of shear rate and (**b**) shear elastic and loss moduli as a function of shear stress for inks of varying composition: (green) 10 wt% monomer solution, (black) 10 wt% monomer solution with 10 wt% nanoclay particles, and (blue) 10 wt% monomer solution, 10 wt% nanoclay, and 0.8 wt% cellulose fibrils.
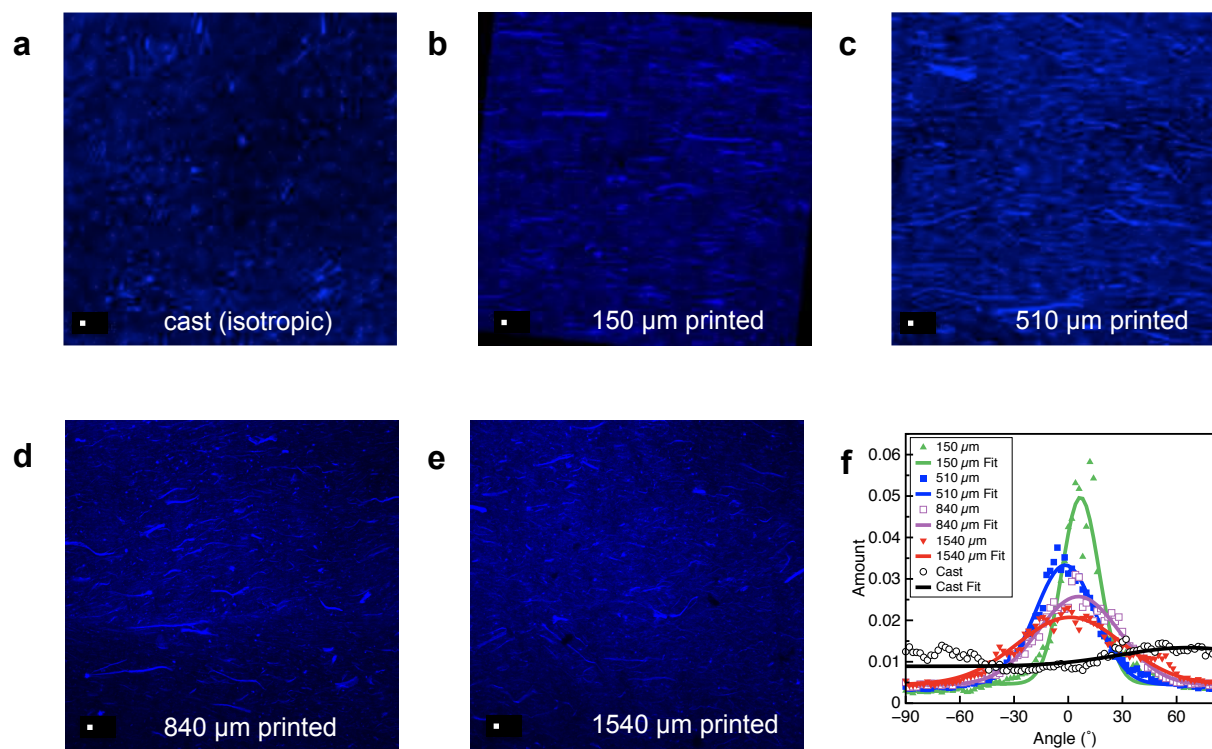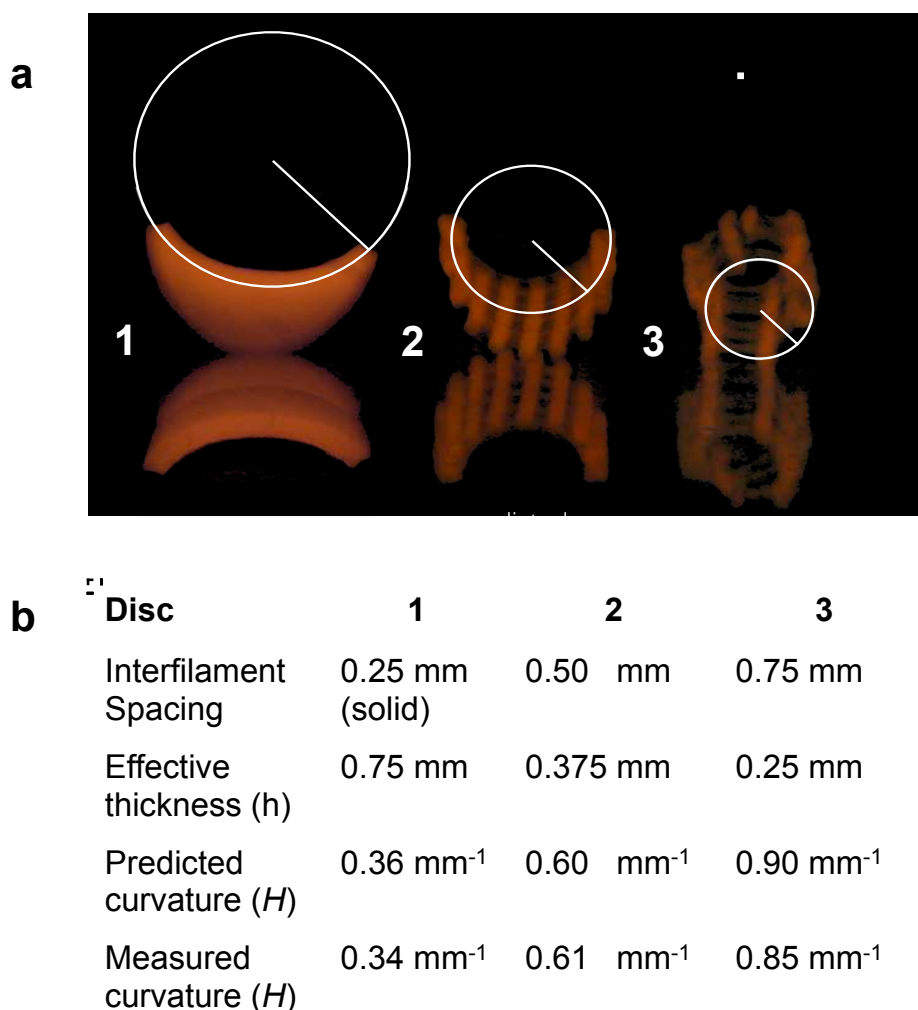
Supplementary Figure 4 | Maximum intensity projection images of Calcofluor White stained samples, obtained by confocal microscopy. **a-e,** isotropic (cast) specimen (**a**), and unidirectional printed samples printed with nozzles of varying diameter: 150 μm (**b**), 510 μm (**c**), 840 μm (**d**) and 1540 μm (**e**). Scale bars = 100 μm. **f,** Fourier transform analysis of confocal images for cast and printed samples.
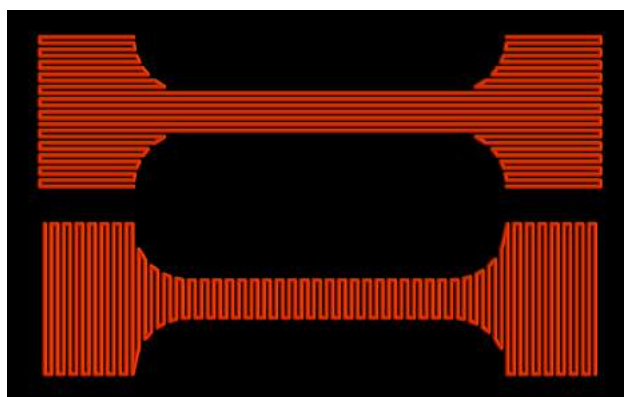

Supplementary Figure 5 | Print path of longitudinal (top) and transverse (bottom) tensile specimens.

a — Stress (Pa) vs Strain (mm/mm) plot with legend:
- Swollen Transverse
- Swollen Longitudinal
- As Fabricated Transverse
- As Fabricated Longitudinal

b

|	Young's Modulus (KPa)	Strain to Failure (%)
As fabricated Longitudinal	1267 ± 201	67 ± 11
As fabricated Transverse	1011 ± 39	140 ± 24
Swollen Longitudinal	41 ± 13	149 ± 10
Swollen Transverse	20 ± 3	320 ± 4

Supplementary Figure 6 | a, Representative tensile stress-strain curves of as-printed (dashed lines) and swollen (solid lines) longitudinal and transverse tensile specimens. **b,** Resulting directional elastic moduli and strain to failure for printed specimens. [Nozzle size = 510 μm.]

a

b

Disc	1	2	3
Interfilament Spacing	0.25 mm (solid)	0.50 mm	0.75 mm
Effective thickness (h)	0.75 mm	0.375 mm	0.25 mm
Predicted curvature (H)	0.36 mm^{-1}	0.60 mm^{-1}	0.90 mm^{-1}
Measured curvature (H)	0.34 mm^{-1}	0.61 mm^{-1}	0.85 mm^{-1}

Supplementary Figure 7 | Observed and predicted curvatures for a series of $90°/0°$ bilayer lattices (**a,** overall diameter of 5 mm) with varying interfilament spacing, printed using a 250 μm nozzle after immersion in water [Scale bar = 2.5 mm]. **b,** Varying the printed interfilament spacing leads to a change in overall lattice porosity, which can be approximated as an effective thickness (h). These thicknesses can be applied to our theory for mean curvature [$H = 3/4(\alpha_1 - \alpha_2)/h = 0.45/h$ mm^{-1}], resulting in good experimental agreement.
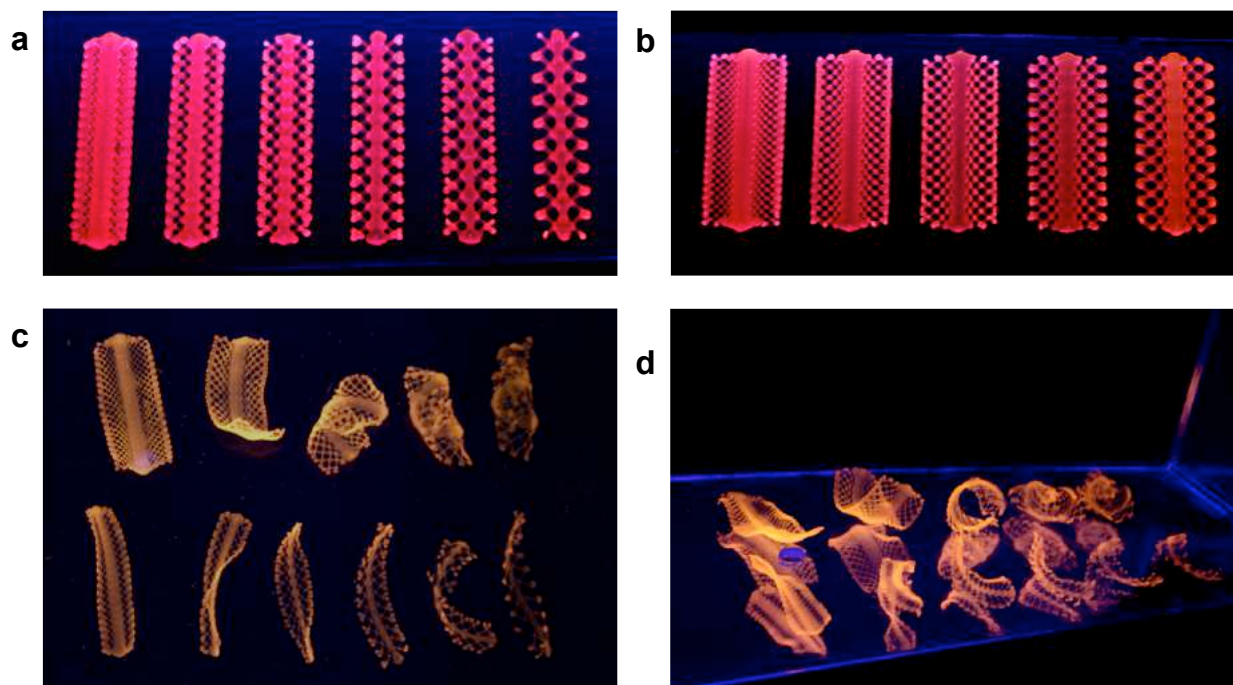
Supplementary Figure 8 | Effect of printed interfilament spacing on curvature of ruffled petal from printed orchid architecture. **a,b,** High aspect ratio (**a**) versus lower aspect ratio (**b**) printed samples, where samples are increasing in interfilament spacing from left to right. [Nozzle size = 250 μm]. **c,d,** Top down (**c**) and side view (**d**) images of samples after swelling, indicating increase in curvature as interfilament spacing increases.

Control (no NFC) Filled (with NFC)

Side view

Top down
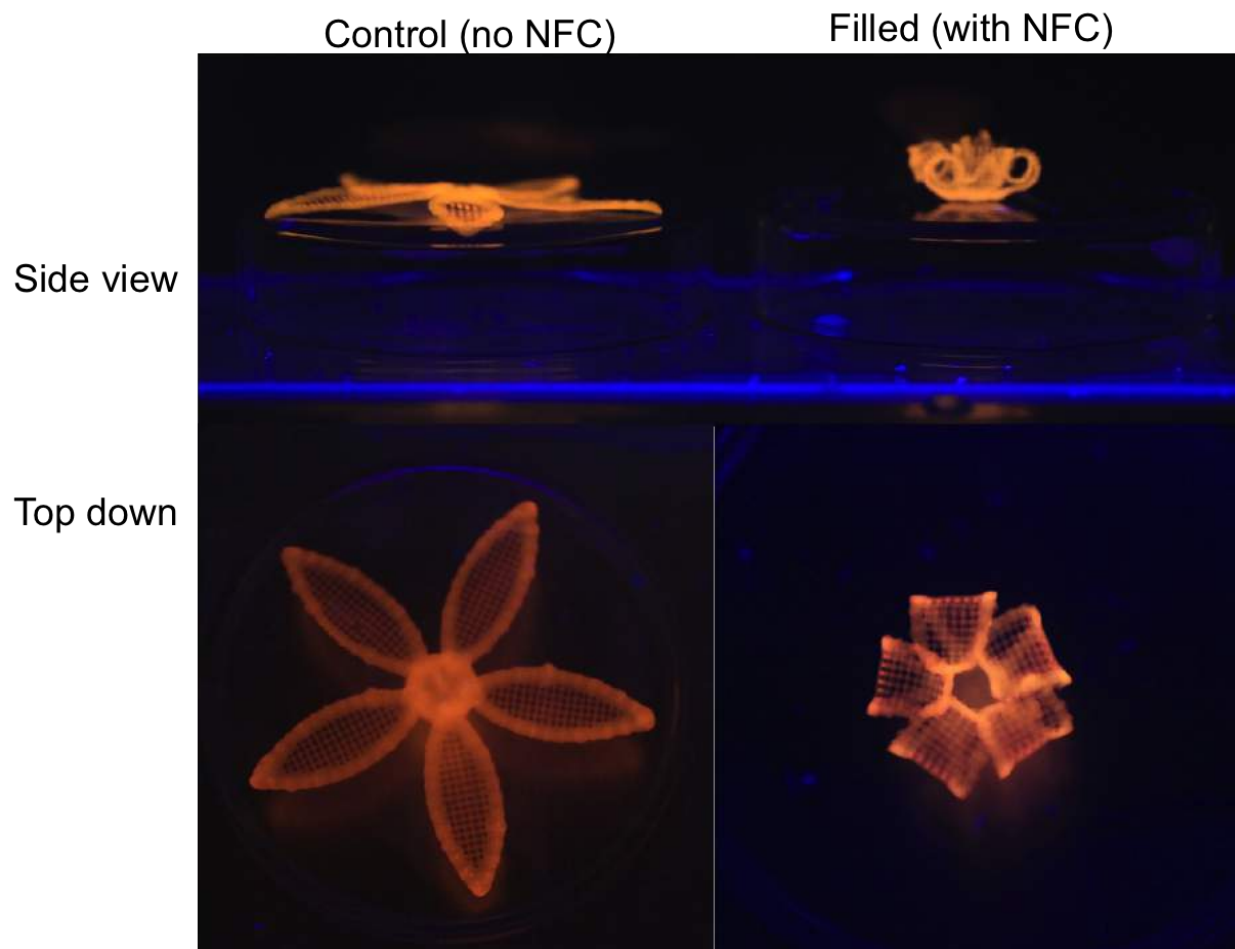
Supplementary Figure 9 | Control flower architecture composed of hydrogel ink with 0 wt% (left), compared to flower architecture (right) with 0.8 wt% NFC. Both flowers are printed using a 200 μm diameter nozzle. Images taken after 24 h immersion in water.
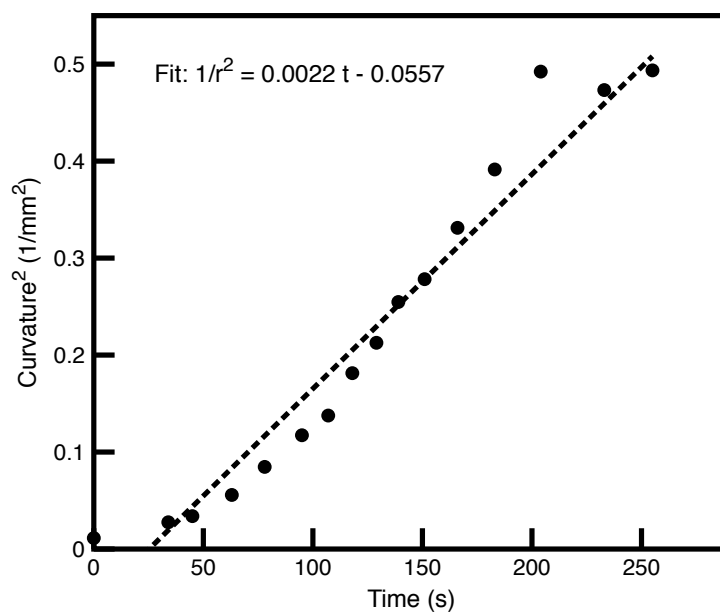
Supplementary Figure 10 | Tracking curvature over time in the 90°/0° flower bilayer demonstrates a roughly diffusion-limited behaviour.
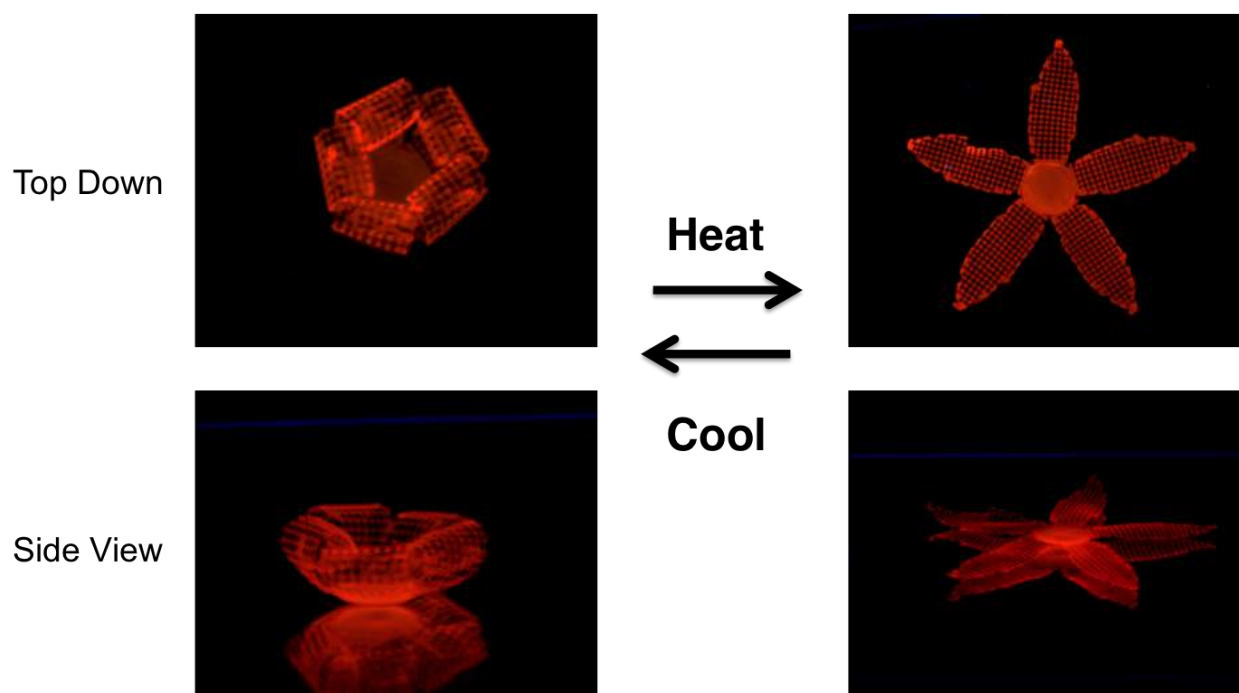
Supplementary Figure 11 | Thermoreversible shape change is exhibited in a 90°/0° flower composed of a poly(N-isopropylacrylamide) (PNIPAm) hydrogel matrix with 0.8 wt% NFC. The structure first reaches equilibrium in room temperature water (left), and upon immersion in a warm water bath (50 °C) the coil-to-globule transition of the PNIPAm results in a contraction of the hydrogel matrix and thus a return to the flat configuration (right). This transformation can be cycled back and forth by changing water temperature. Top down views (above) compared to side views (below). Nozzle size = 250 μm.
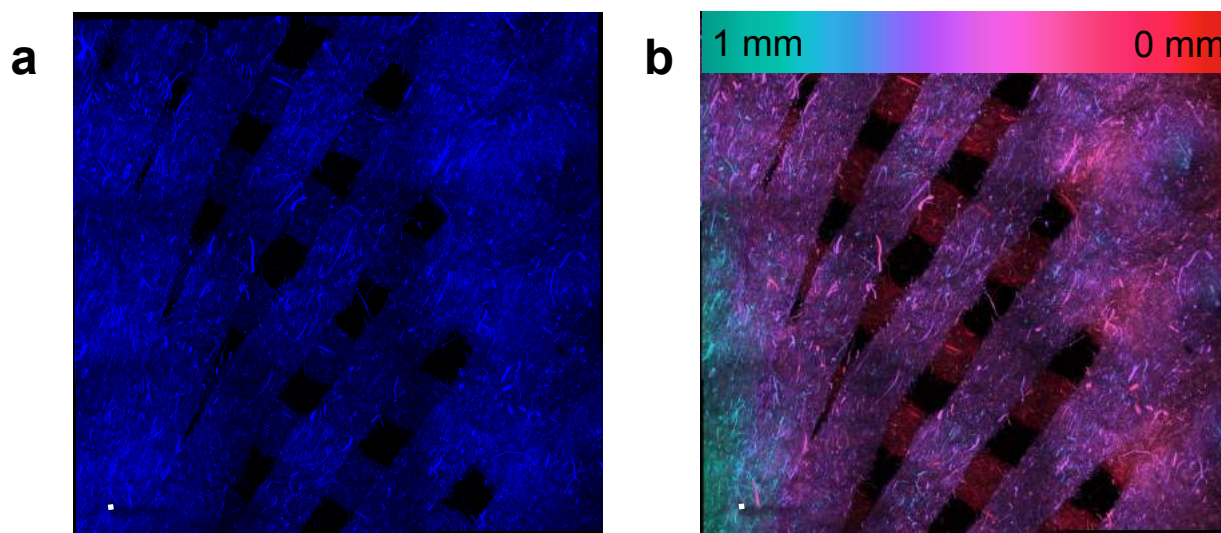
Supplementary Figure 12 | **a,** Confocal microscopy Z-stack image of stained NFC in ruffled petal from orchid architecture (nozzle size = 250 μm), maximum intensity projection. **b,** Confocal microscopy Z-stack image, showing the 3D nature of the structure via height colour mapping, maximum intensity projection. Scale bar = 500 μm.
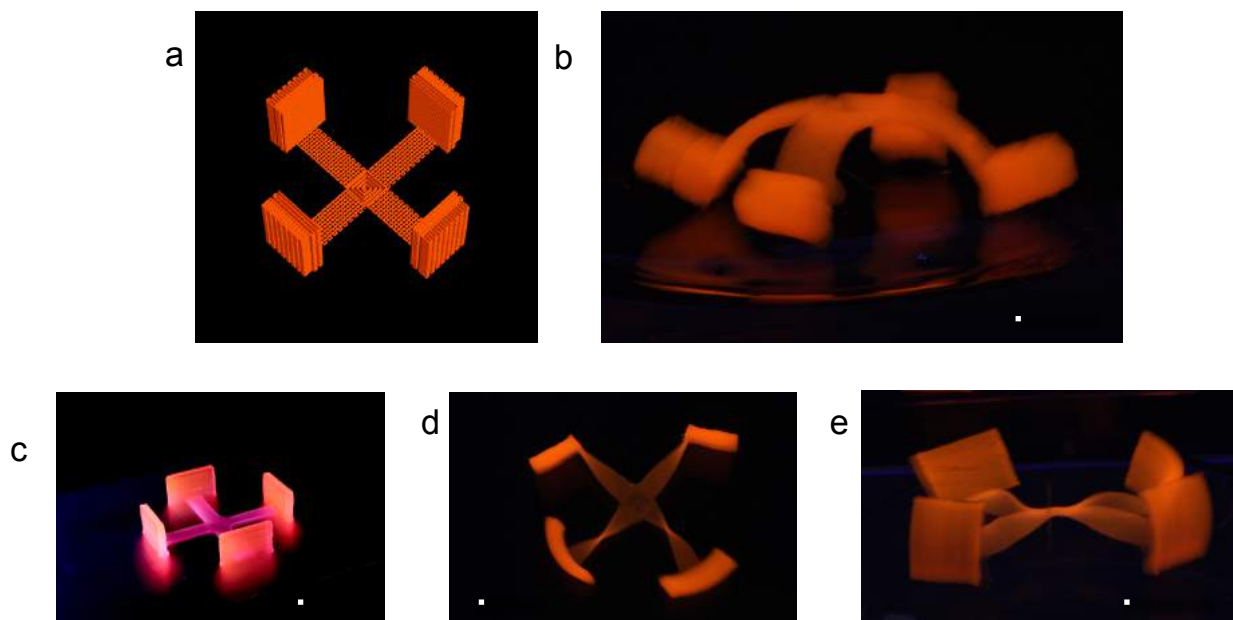
Supplementary Figure 13 | Shape changing architectures with 3D shape changing elements can be produced with bio-4DP. **a,** Schematic of 3D print path: Pillars contain 24 layers of ink, comprised of a vertical bilayer of longitudinal and transverse meander paths, resulting in a saddle like transformation. Bottom X-beam (connecting the pillars) can contain any bilayer configuration: here we show $90°/0°$(**b**, 510 μm nozzle) and $-45°/45°$(**c-e**, 250 μm nozzle). **c,** As-fabricated $-45°/45°$3D structure, with top views (**d**) and side views (**e**) of the transformed structure. [Scale bars = 10 mm]

Supplementary Video 1 | Video of shape change in water for overlapping arcs architectures represented in Fig. 2d, created via time-lapse images [Scale bar = 10 mm, nozzle size = 250 μm, total time $\approx$ 7 minutes].

Supplementary Video 2 | Video of shape change in water for flower architecture with $90°/0°$ bilayer orientation, created via time-lapse images [Scale bar = 5 mm, nozzle size = 200 μm, total time $\approx$ 5 minutes].

Supplementary Video 3 | Video of shape change in water for flower architecture with $-45°/45°$ bilayer orientation, created via time-lapse images [Scale bar = 5 mm, nozzle size = 250 μm, total time $\approx$ 25 minutes].

Supplementary Video 4 | Video of reversable shape change for NIPAm-NFC flower of $90°/0°$ bilayer orientation placed in a heated water bath (40 °C), created via time-lapse images [Scale bar = 5 mm, nozzle size = 200 μm, total time $\approx$ 30 minutes].

Supplementary Video 5 | Video of printing process for orchid architecture. In bright field, the ink appears translucent pink [nozzle size = 250 μm].

Supplementary Video 6 | Video of shape change in water for orchid-mimicking flower architecture, created via time-lapse images [Scale bar = 5 mm, nozzle size = 250 μm, total time $\approx$ 20 minutes].

Supplementary Video 7 | Video of printing process for calla lily architecture. UV lighting was used to excite fluorescent rhodamine dye [nozzle size = 410 μm].